Design of Hydraulic Power Take-Offs for Wave-Powered Reverse Osmosis Desalination: Meeting Constraints on Pressure Variation

Jeremy Simmons and James Van de Ven

1 Introduction

Researchers and government agencies have recently turned their attention toward renewable energy, such as solar, wind, and ocean wave energy, as direct sources of power for desalination of seawater [1, 12, 16, 18]. There is specific interest in reverse osmosis (RO) [13, 14]. This is a membrane-based process used to separate water from dissolved solids using high pressure as a driving force that is three to six times more energy efficient than thermal desalination processes. As a way to reduce cost and improve the efficiency of a wave-powered RO process, the reverse osmosis process can be integrated into the hydraulic circuit of a wave energy converter's (WEC) power take-off (PTO) (the subsystem responsible for loading the WEC and converting power) [3, 10, 18, 20, 29]. This avoids losses in the conversion of power to and from mechanical and electrical power when pressurizing feedwater.

An example architecture for a wave-powered reverse osmosis system is shown in Fig. 1. This system is capable of co-generating fresh water and electricity. This system includes (1) a seawater compatible pump that is driven directly by the oscillating WEC, (2) an RO membrane module receiving pressurized seawater from the WEC-driven pump, (3) an energy recovery unit (ERU) that recovers available power from the waste brine stream of the RO module and drives additional seawater to the RO feed inlet, (4) a charge pump that drives an intake flow and provides an elevated pressure at the WEC-driven pump inlet (to avoid cavitation), and (5) a hydraulic motor and electric generator that produce electrical power for onsite electrical power consumption and to regulate the mean pressure at the RO feed inlet. Additional components for this system that are not shown are pressure relief valves (PRVs) used to limit peak pressures.

J. Simmons · J. Van de Ven (✉)
University of Minnesota, Minneapolis, MN, USA
e-mail: vandeven@umn.edu

L. Ericson and P. Krus (eds.), *Advancements in Fluid Power Technology: Sustainability, Electrification, and Digitalization*, Lecture Notes in Mechanical Engineering,
https://doi.org/10.1007/978-3-031-84505-5_16

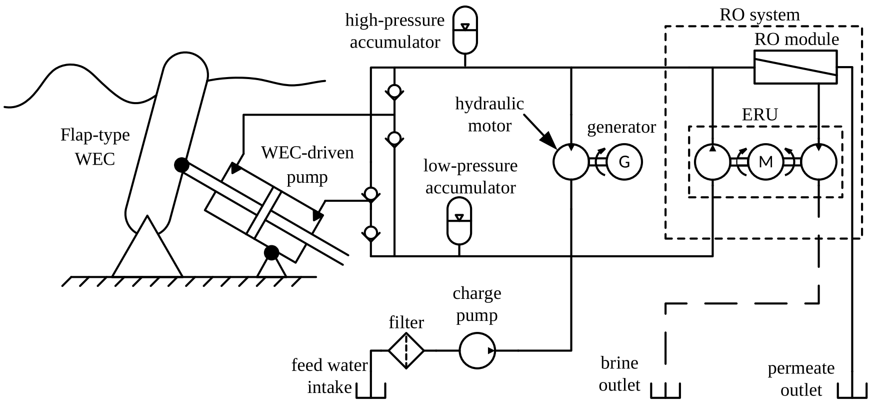

Fig. 1 A wave-powered reverse osmosis (RO) system comprised of a flap-type wave energy converter (WEC) and hydraulic power take-off operating with seawater as the working fluid to produce fresh water (Figure adapted from [23, 24])

Conversion of wave energy is a considerable technical challenge. The wave energy conversion process is a characteristically variable process. It involves absorbing power under the force of slow, irregular waves with a high degree of variation. For example, the ratio between the peak and mean power absorbed by a WEC has been estimated to be anywhere between 7 and 58 to 1, depending on the system design and load control scheme [15, 26]. In contrast, the conventional RO process is characteristically steady, with changes to operation being made very slowly and only as feedwater temperature changes or the membrane performance degrades. In fact, several sources recommend that start-up and shut-down of RO systems should be performed relatively slowly, with a rate of change in pressure less than 70 kPa per second, to avoid mechanical damage to the membrane and membrane housing [8, 17, 27].

The recommended limit to the rate of change in feed pressure is of particular interest in this work because it is a dominant constraint in the selection of accumulator volumes. This constraint is specified for start-up and shut-down without an extension to normal operation being made explicit by the literature. However, in normal operation of conventional RO systems, the pressure is held nearly constant, so it is understandable that an explicit statement would not be made. Furthermore, the value of the constraint seems not to be substantiated in any literature. The lack of clarity on this issue suggests that the constraint may be conservative, based on experience, and/or that the underlying mechanisms of failure motivating the constraint are not well understood. However, both [17, 27] claim that this constraint relates to mechanical damage to the membrane and membrane housing and suggest compaction of the membrane and cracking of the housing to be modes of failure.

Early work on wave-powered RO systems has dismissed this constraint. In the work by Folley et al., the constraint was acknowledged but neglected for lack of substantiation in literature and based on an argument that more robust RO system components would be produced if a wave-powered RO industry created the demand [11].

Recently, work by Sitterly et al. [25] and Das et al. [7] have acknowledged a potential for the pressure variations in wave-powered RO systems to harm RO membranes. Both works studied the effect of pressure variation using an experimental system with pressure being controlled. Sitterly et al. controlled pressures to match numerical results of a wave-powered RO system model presented in [29]. As part of their analysis, the authors compared the performance of the RO module before and after the membrane elements were subjected to the pressure variation experiments. They reported a decrease in membrane permeability of 7.4% and a decrease in water flux of 18.4%. It is important to note that this change came after a standard break-in procedure where membrane compaction is expected. The authors hypothesized that the pressure variation drove additional compaction that would not have occurred otherwise. The conclusion was that the pressure variation did not have significant effects on the membrane performance and integrity. However, from a system-level perspective, having membrane productivity decline 18.4% is substantial.

Das et al. [7] controlled pressure in two ways: first as sinusoidal variations between 35 and 65 bar and then as rectified sinusoidal functions with pressure varying between 0 and 70 bar. Membrane integrity tests showed no significant change after the simple sinusoidal pressure tests. However, after the more extreme rectified sinusoidal tests, the membrane integrity tests showed a two to four times increase in the salinity of the permeate suggesting significant degradation of the membranes' integrity.

This paper addresses the design impacts associated with meeting the pressure rate-of-change constraint on several alternative PTO architectures. Design performance is evaluated by two design metrics: the total volume of accumulators deployed and the amount of power lost during operation. The baseline architecture is also evaluated without the rate-of-change constraint enforced. Each architecture is modeled mathematically and numerically simulated to estimate its performance. Grid studies are used to find optimal values for the design parameters relevant to each architecture.

The proposed architectures are described in the following section, Sect. 2. The methods of this study are described in Sect. 3 and include the mathematical models, the method of solving the models, and the procedure for optimizing and comparing the design performance of each architecture. The results of the study are presented in Sect. 4 and are followed by a discussion and suggestions for future work in Sect. 5. Conclusions drawn from the study are presented in Sect. 6.

2 Proposed Power Take-Off Architectures

The baseline architecture for this design study, shown in Fig. 1, includes a first-order low-pass filter in the form of a single high-pressure accumulator. A second-order low-pass filter is easily constructed with the addition of a resistive element and a second accumulator as shown in Fig. 2a. The resistive element could be a passive element

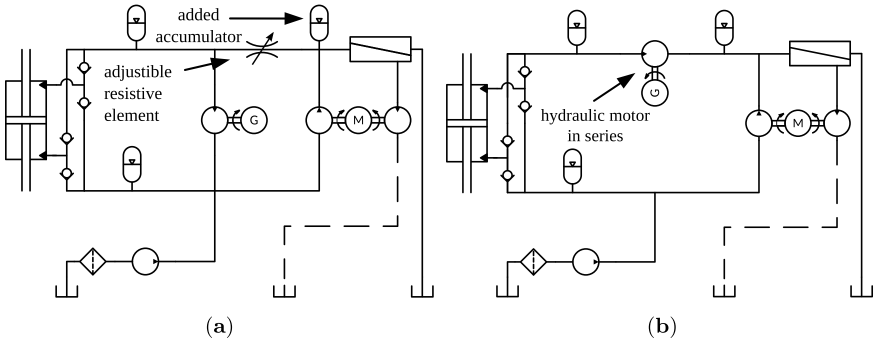

Fig. 2 Proposed PTO architecture schematics: (**a**) a parallel-type power take-off architecture with a second-order low-pass filter (**b**) and a series-type power take-off architecture (figure adapted from [23])

or an actively controlled valve. The passive element accomplishes the formation of a second-order low-pass filter while an actively controlled valve provides the opportunity of controlling the flow to the RO feed inlet and thereby rate of change in pressure. Both approaches reduce the total accumulator volume required to meet the pressure rate-of-change constraint.

A third alternative is the series-type PTO architecture proposed in [23] and illustrated in Fig. 2b. In this architecture, the hydraulic motor of the parallel-type architecture is placed in series with the WEC-driven pump and RO module. This way the hydraulic motor, which can operate as either a motor or a pump, has direct control of the flow reaching the RO feed inlet from the WEC-driven pump.

3 Methods

The goals of this work are to (1) understand how the selection of architecture influences the required accumulator volume and energy losses in the system when the rate-of-change constraint is enforced and (2) understand how volume requirements compare when the constraint is not enforced. The metric assumed for energy losses is the average power losses associated with managing the pressure variation; specifically, the losses from the activation of pressure relief valves at the outlet of the WEC-driven pump and the feed inlet of the RO module, the power losses from the hydraulic motor and electric generator, and throttling losses of the resistive element.

Numerical models of the system are used to simulate the system and perform a grid search to identify optimal performing designs for each PTO architecture. The design variables considered in the grid search (where applicable) are the total high-pressure accumulator volume, the proportion of volume placed at the RO feed inlet (versus the outlet of the WEC-driven pump), and the resistance of the resistive element.

To identify the cost of the constraint to the design performance, the optimal design performance for the baseline architecture is evaluated with and without enforcing the constraint on pressure rate of change.

The hypothetical system being considered is one installed in the nearshore environment at Humboldt Bay, CA and which is being driven by the Oyster 1, a bottom hinged flap-type WEC (like the one illustrated in Fig. 1) designed and tested by the former Irish company Aquamarine Power [2]. This selection of site and WEC design builds on prior work on wave-powered RO [23, 28]. The displacement of the WEC-driven pump and RO membrane area are selected based on the design study presented in [23]. The parameters are selected from the parallel-type and series-type PTO architecture having a fixed pump displacement and fixed RO membrane area and are based on having the same RO membrane area and annual rate of freshwater production.

A single sea condition is evaluated which is selected from the sea states specified for the Wave-to-Water Prize competition [5]. The selected sea state from that set, having a significant wave height of 2.64 meters and a peak period of 9.86 s, contributes the most to the annual available wave energy and when taken as a corner condition (maximum sea height and wave period), accounts for approximately half of the available wave energy annually (this is based on data from a near shore buoy in Humboldt Bay, CA for the rate of occurrence of sea states [28] with a weighting by available wave power).

The following subsections present the mathematical models used to simulate the WEC and proposed PTO architectures, the control methods, the method of solving the numerical problem of simulating the system, and the procedures used to carry out the design study.

3.1 Modeling

The WEC/PTO systems are modeled as being a dynamic system, described by a set of ordinary differential equations. The WEC and PTO subsystem models are coupled. The velocity of the WEC is an input to the PTO subsystem model and the reaction torque of the WEC-driven pump is an input to the WEC subsystem model. The inputs to the WEC subsystem model are the surface elevation of the ocean waves around the WEC and excitation force of the waves on the WEC.

Wave Energy Converter Model The model of the WEC and the parameters used in the study are identical to those developed by the authors in [23]. The state variables describing the WEC subsystem are the position and velocity of the WEC, and a set of states describing the forces on the WEC due to wave refraction.

The forces on the WEC include the wave excitation force, radiation damping, a hydrostatic restoring force, and weight of the device. The wave elevation and excitation force are constructed from the Pierson-Moskowitz spectrum [9] using the superposition of 1000 sinusoidal signals having frequency dependent amplitudes and phase. The phase of each frequency component is additionally modified by a uniformly distributed random value in the range $[-\pi, \pi]$. Frequency components are distributed based on an equal energy method such that each interval of the wave elevation power spectrum has an equal area. The frequency dependent coefficients for the amplitude and phase were obtained using the open source boundary element method solver Nemoh [6], as was an impulse response function for the radiation damping. The methods presented in [21] were used to identify a 3rd order system model approximating the impulse response function.

Power Take-Off Model Each PTO architecture shares several components that are modeled identically. The differences between the PTO models are in the parameter values of the model (specifically the WEC-driven pump displacement and the hydraulic motor displacement), the flow connections, and the control algorithms applied.

A schematic showing the modeled variables and node connections for these PTO architectures is given in Fig. 3. This schematic accounts for each architecture with the optional configuration displayed with dashed-line boxes. For the baseline architecture, the added resistive element and additional accumulator associated with the pressure p_f are excluded. For the parallel-type architectures, the hydraulic motor discharges to the low-pressure branch. For the series-type PTO architecture, it discharges to the RO feed inlet. The low-pressure branch, which includes the charge pump and low-pressure accumulator, were included in the model but are not described here because they have little effect on the behavior of the high-pressure branch. The pressure of the low-pressure branch in every simulation was approximately constant at 0.44 MPa.

The state variables for these PTO models are the pressures at nodes having compressible volumes and the integral of the error for a proportional-integral pressure regulating controller determining the shaft speed of the electric generator.

The derivatives of pressure states are a function of the capacitance of the node, the net flow into the node, and changes to the fluid volume:

$$C_i\left(p_i\right)\frac{dp_i}{dt} = \sum q_{in} - \sum q_{out} - \frac{dV_i}{dt} \tag{1}$$

where p_i is the pressure of node i, $C_i\left(\cdot\right)$ is the nonlinear function describing the capacitance of the node as a function of pressure, q_{in} and q_{out} are flowrates into and out from the node, respectively, and V_i is the volume of the node.

The pumping chambers of the WEC-driven pump are modeled as volumes of compressible fluid. The working fluid is assumed to be a mixture of seawater and entrained gas with the properties given in Table 1. The seawater is assumed to be linearly compressible while the entrained gas is modeled as an ideal gas compressed isothermally. Therefore, the capacitance of these volumes is described by

$$C_{f,i}\left(p_i\right) = \frac{V_i\left(1 + \beta\alpha\frac{p_o}{p_i^2}\right)}{\beta} \tag{2}$$

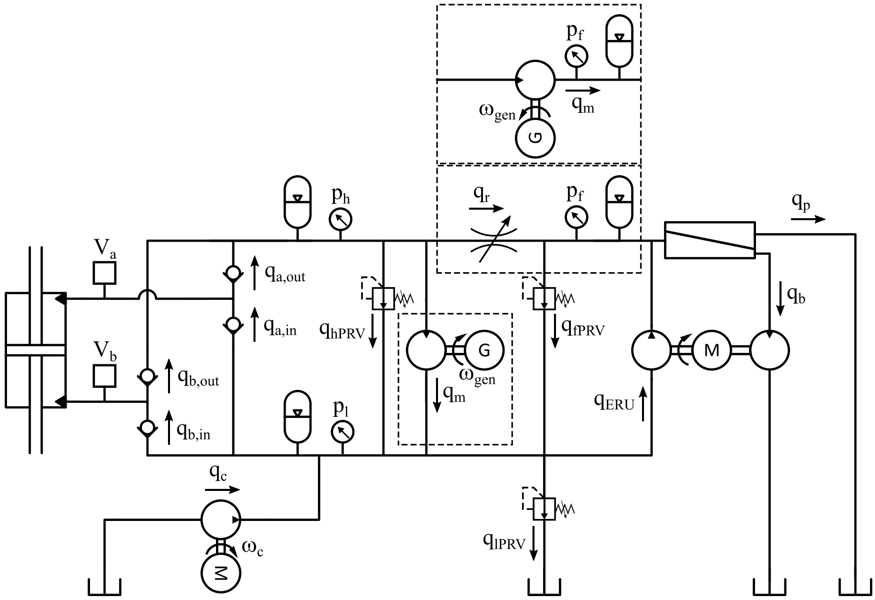

Fig. 3 Modeling schematic with optional configurations (i.e., with resistive element and additional accumulator and parallel-type or series-type architecture) are indicated with dashed line boxes

Table 1 Working fluid parameters

Parameter	Value	Units
Density, ρ	1025	kg/m^3
Viscosity, dynamic, μ	$9.4\cdot10^{-4}$	Pa·s
Bulk modulus, β	$2.2\cdot10^{9}$	Pa
Entrained air fraction (at 1 atm), α	0.0001	–
Atmospheric pressure	101300	Pa

where β is the bulk modulus of the liquid phase (i.e., seawater) and α is the volume fraction of entrained air at the reference pressure, p_o. The volume of each pumping chamber is a function of the WEC position and is assumed to change proportionally with the position of the WEC. The maximum extent of the WEC-driven pump is assumed to be at $\pm\pi/2$ radians from the vertical position of the flap-type WEC. An additional dead volume, equal to 10% of the total swept volume, is added to each pumping chamber to account for non-swept volume such as porting and piping.

The accumulators are modeled as being ideal gas volumes being compressed isothermally:

$$C_{g,i}\left(p_i\right) = V_{c,i}\frac{p_{c,i}}{p_i^2} \tag{3}$$

where p_c and $V_{c,i}$ are reference values for pressure and volume of the gas at node i.

The flow through the resistive element of the pressure filter and the check valves of the WEC-driven is modeled as flow through an orifice such that

$$q_i\left(\Delta p_i\right) = k_{v,i}\frac{\Delta p_i}{\left|\Delta p_i\right|}\sqrt{\left|\Delta p_i\right|} \tag{4}$$

where $k_{v,i}$ is a flow coefficient for valve i, Δp_i is the difference between the upstream and downstream pressure. There is no flow through the check valves when the pressure differential is below the cracking pressure and there is a pressure margin over which the area of the valve increases with the pressure differential until it is fully open. For the marginal regime, the flow coefficient for the check valves is assumed to vary linearly with the pressure difference between zero and the maximum value. Parameters for the check valves are given in Table 2.

The pressure relief valves are modeled with a flow coefficient varying linearly with poppet position (assuming a force balance between static pressure acting on the poppet faces and a linear spring, as was assumed in [23]) giving the flow rate

$$q_i = \frac{1}{C_{prv,i}}\left(p_i^{\frac{3}{2}} - p_{cr,i}\,p_i^{\frac{1}{2}}\right) \tag{5}$$

where, for valve i, $p_{cr,i}$ is the cracking pressure and $C_{prv,i}$ is determined by a desired peak flowrate and peak pressure. The parameters used for the pressure relief valves are given in Table 3.

Table 2 WEC-driven pump check valve parameters

Parameter	Value	Units
Cracking pressure	$1{\cdot}10^5$	Pa
Margin to fully open	$1{\cdot}10^5$	Pa
Flow coefficient, inlet	15.18	L/Pa$^{1/2}$
Flow coefficient, outlet	10.11	L/Pa$^{1/2}$

Table 3 Pressure relief valve parameters

Parameter	Value	Units
PRV at WEC-driven pump outlet		
Cracking pressure, $p_{cr,hPRV}$	$20{\cdot}10^6$	Pa
Coefficient, $C_{prv,hPRV}$	$2.2361{\cdot}10^9$	Pa$^{3/2}$·s/m^3
PRV at RO feed inlet		
Cracking pressure, $p_{cr,fPRV}$	$8.3{\cdot}10^6$	Pa
Coefficient, $C_{prv,fPRV}$	$1.4405{\cdot}10^9$	Pa$^{3/2}$·s/m^3

Mechanical and flow losses of the hydraulic motor are modeled using the McCandlish-Dory model [19] with constant coefficients and fixed displacement. The flow rate through the pump/motor is modeled as

$$q_m = D_m \omega_m \left(1 - \lambda \left(C_s \frac{|\Delta p|}{\mu |\omega_m|} + \frac{\Delta p_i}{\beta} (V_r + 1)\right)\right) \tag{6}$$

where D_m is the volumetric displacement per radian, ω_m is the shaft speed in radians per second, μ is the dynamic viscosity of the working fluid. The torque of the motor and generator are modeled as

$$T_m = D_m \Delta p \left(1 + \lambda \left(C_v \frac{\mu |\omega_m|}{|\Delta p|} + C_f\right)\right) \tag{7}$$

The coefficients of Eqs. 6 and 7 are given in Table 4.

The WEC-driven pump and electric generator are assumed to have a fixed efficiency with values in Table 4. The WEC-driven pump displacement is derived from results in [23]. The displacement of the hydraulic motor was chosen for the parallel-type architecture based on a grid study considering the performance of the pressure regulation and the power losses of the motor, generator, and pressure relief valves; this study is presented in [22]. For the series-type architecture, it was chosen to provide the flowrate required to achieve steady operation of the RO module at 8 MPa.

Table 4 WEC-driven pump, hydraulic motor and generator parameters

Parameter	Parallel-type	Series-type	Units
WEC-driven pump			
Displacement	0.23	0.163	m^3/rad
Efficiency, mechanical	0.9		–
Hydraulic motor and generator			
Generator efficiency	0.9		–
Maximum speed	1750		rpm
Motor displacement,	1000	2300	cc/rev
Laminar flow loss coefficient, C_s	$3.0554 \cdot 10^{-10}$		–
Volume ratio, V_r	1.103		–
Viscous torque loss coefficient, C_v	$7.1755 \cdot 10^{5}$		–
Coulomb torque loss coefficient, C_f	0.0259		–

Table 5 Reverse osmosis module and energy recovery unit (ERU) parameters

Parameter	Value	Units
Membrane area, S_{ro}	3,700	m^3
Permeability coefficient, A_{perm}	$2.57 \cdot 10^{-12}$	$m^3/(N \cdot s)$
Recovery ratio	0.25	–
ERU Volumetric efficiency	0.95	–
ERU Mechanical efficiency	0.95	–

The rate of permeate production by the RO module is modeled as

$$q_p = S_{ro} A_{perm} \left(p_f - p_{osm} - p_p \right) \tag{8}$$

where p_{osm} is the osmotic pressure of the seawater solution, p_p is the pressure at the permeate outlet, S_{ro} is the total installed membrane surface area, and A_{perm} is a coefficient describing the permeability of the membranes. The seawater is assumed to have an osmotic pressure of 2.275 MPa. The permeate outlet pressure is assumed to be atmospheric pressure. The permeability coefficient is taken from [29], which is based on results of the WAVE design tool offered by FilmTec for a particular configuration of RO membrane elements [4].

The ERU is assumed to maintain a constant recovery ratio in the RO process of 25% (i.e., the ratio of permeate production to feedwater intake), which is achieved by controlling the ERU shaft speed. Mechanical and volumetric losses from the ERU's hydraulic motor and pump are modeled with constant efficiency. The electric motor makes up for the difference in torque between the hydraulic motor and pump. The hydraulic motor and pump are assumed to have the same volumetric displacement. Parameters used for the RO module and ERU are given in Table 5.

Control There are two control schemes implemented for the PTO subsystem. First, the hydraulic motor and generator are used to regulate the RO feed pressure using a feed-back control loop. Second, the flow coefficient for the active resistive element is used to limit the rate of change in feed pressure. In this case, the flow coefficient is prescribed by feed-forward control.

Proportional-integral control is used for pressure regulation. The error is the difference between the pressure at the RO feed inlet and the nominal set point. The control signal is a nominal shaft speed for the generator. For the parallel-type PTO architectures, only the proportional term is used. The proportional and integral terms are both used for the series-type PTO architecture. The value for the proportional gain in both cases is $5 \cdot 10^{-4}$ rad/s/Pa. The integral gain is $5 \cdot 10^{-6}$ rad/s^2/Pa.

The feed-forward control specifying the flow coefficient of the resistive element is based on a model for the pressure node capacitance and the flowrates associated with the RO module. In practice, the model would have to estimate these values and may include an observer that is informed by sensor measurements. For this study, these values are calculated by reversing the calculations given above. The feed-forward control identifies an ideal flow coefficient based on a positive rate of change in feed pressure equal to the prescribed limit. The flow coefficient command is bound by an upper bound attributed to the size of the valve. The ideal flow coefficient is

$$k_{v,ideal} = \frac{p_h - p_f}{|p_h - p_f|} \frac{C_f\left(p_f\right) + q_f - q_{ERU,f}}{\sqrt{p_h - p_f}} \tag{9}$$

3.2 Numerical Solution

These models are solved using the Euler method with a time step of $5 \cdot 10^{-6}$ seconds. This time step was selected based on convergence of a mass and energy balance. Similarly, the length of time simulated is based on a convergence study on the power captured by the WEC and metrics of pressure variation (i.e., mean, minimum, maximum, and variance). The simulations are 2250 s long with only the last 2000 seconds contributing to the performance calculations.

3.3 Design Studies

The PTO architectures are compared based on power losses and the total accumulator volume. The Pareto front is approximated using a multi-variable grid study. The pressure rate-of-change constraint is enforced through eligibility to the Pareto optimal set.

The variables of each grid study are specified in Table 6. Total volume refers to the total volume for the high-pressure accumulators. The distribution of volume between the accumulator upstream and downstream is indicated by the proportion of the total volume placed at the RO feed inlet. Along with the range of values, the number of grid points and the distribution scheme for the grid points are specified. Two grid

Table 6 Grid study parameters: bounds, number of grid points and spacing scheme

PTO architecture	Total volume	Portion at RO feed	Flow coefficient
	(L)		(L/kPa$^{1/2}$)
Baseline	500–30,000 (80/log)	–	–
Passive element, with constraint	5,000–15,000(10/log)	0.2–0.35(10/equal)	0.1–15(40/log)
Passive element, without constraint	1,000–15,000(80/log)	0.05–0.9(10/equal)	0.1–30(20/log)
Active element	5,000–15,000(10/log)	0.01–0.99(40/equal)	40(1/–)
Series-type	1,000–15,000(20/log)	0.01–0.95(40/log)	–

point distribution schemes are used; a constant spacing between grid points and a log-scale spacing.

4 Results

In this section, results are presented from the grid study for the baseline case, a comparison of the Pareto optimal performance results for each PTO architecture, and time-series results for the proposed PTO architecture with representative selections of design parameters.

Grid study results for the influence of accumulator volume on the peak rate of change in feed pressure and mean power loss for the baseline PTO architecture are given in Fig. 4. The mean power losses include the pressure relief valves and the hydraulic motor and generator and are normalized to the mean power capture by the WEC. The lowest total high-pressure accumulator volume meeting the constraint on the pressure rate of change is 17,600 liters. Above 3,000 liters of accumulator volume, power losses are near constant at about 2.8%. The pressure relief valves are not used in this range, only the hydraulic motor and generator contribute to these losses. Below 3,000 liters, the pressure relief valve at the RO feed inlet is activated and increases the losses up to 5.5% with 500 liters of accumulator volume.

The Pareto optimal performance for all the PTO architectures is given in Fig. 5. This figure shows the power losses as a function of the total accumulator volume. Results for the baseline architecture are given without regard for the pressure rate-of-change constraint (indicated by "no constraint" in the legend). However, the minimum volume needed to meet the constraint is indicated with a vertical dash-dotted line.

These data show a clear ranking in the performance of the architectures. First, the parallel-type architecture with the additional resistive-capacitive network performs better with an active element than a passive element. Second, for accumulator volumes less than 8,000 liters, the series-type architecture outperforms the parallel-type architectures. However, above about 8,000 liters, the power losses are greater for the series type architecture; this is due to the losses of the hydraulic motor being greater in the series configuration, at 3.1%, than in the parallel configuration at 2.8%. Third, when the pressure rate-of-change constraint is not enforced, the baseline outperforms all cases where the constraint is enforced.

To compare required accumulator volume between the architectures, a target limit value of 5% loss is considered, which is just less than double the power loss of the baseline architecture with 17,600 liters. At 5% combined power loss, the parallel-type architecture requires 9,090 liters with a passive resistive element and 7,920 liters with an active element. The series-type architecture requires 4,370 liters. Respectively, these values account for reductions in the required volume from the baseline of 48, 55, and 75%. When the pressure rate-of-change constraint is not observed, the baseline architecture requires 670 liters to achieve 5% combined power loss. This is 96% less volume than is required to meet the rate-of-change constraint.

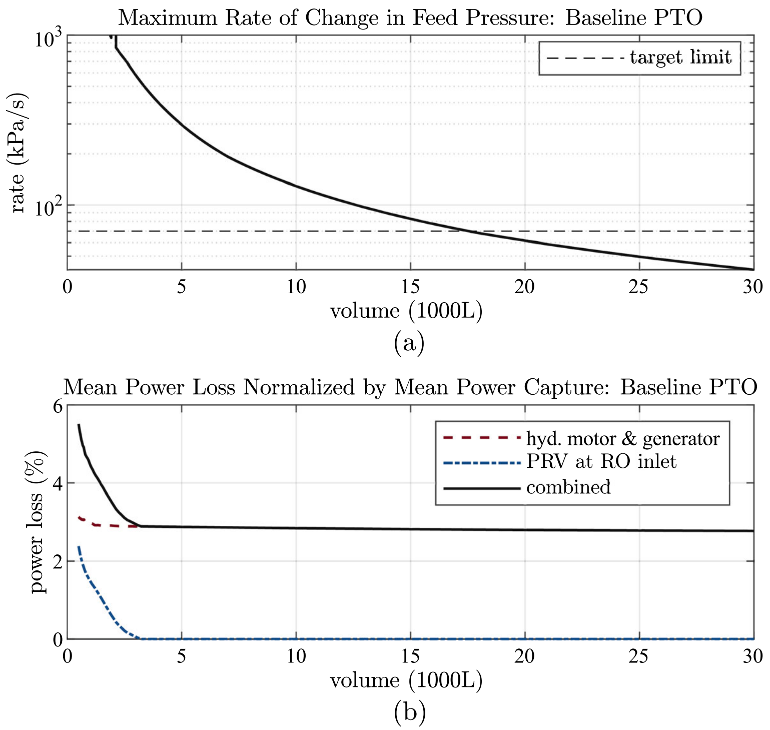

Fig. 4 Grid study results for the baseline PTO architecture: rate of change in feed pressure (**a**) and power loss (**b**)

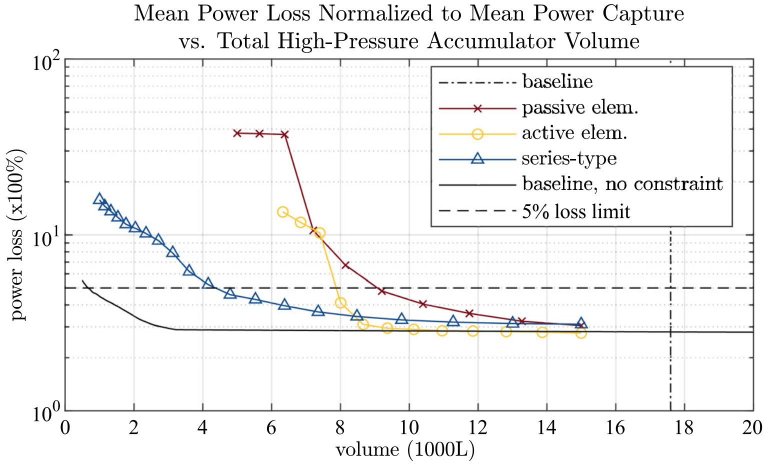

Fig. 5 Comparison of the design performance of each PTO architecture

Permeate production has been left out of this analysis since, by design, the permeate rate should be consistent for all cases. This is confirmed by the results for each design meeting the 5-% combined loss. The baseline produced 1870 m^3/day when meeting the constraint and 1890 m^3/day without. The parallel-type produced 1860 m^3/day with the passive pressure filter and 1900 m^3/day with the active pressure filter. The series-type produced 1850 m^3/day. All values are within 3% difference.

Time-series results related to pressure variation illustrate the behavior of these systems. These are presented for the designs meeting the 5-% combined loss. First, results for the parallel-type architecture with a passive resistive element and 9,090 liters of total volume are given in Fig. 6. The other design parameter values for this case are a flow coefficient of 4.06 L/s/$\mathrm{kPa}^{1/2}$ and 28.3% of the accumulator volume at the RO feed inlet. These results show (1) pressure at the two accumulator banks, (2) the behavior of the hydraulic motor responding to the difference between the nominal RO feed pressure and the actual pressure, and (3) the rate of change in feed pressure compared to the target limit of 70 kPa/s. Two observations are notable. First, there is only a small difference in pressure between the two accumulators (i.e., about 0.14 MPa on average). Second, the rate of change in pressure approaches the peak of 70 kPa/s for only a small fraction of time within the 2000 second simulation. For comparison, the 97th and 99th-percentile values of the rate-of-change magnitude are indicated and are 38 and 48 kPa/s, respectively.

Results for the parallel-type architecture with an active resistive element and 7,920 liters of total volume are given in Fig. 7. This design has 94.7% of the accumulator volume at the RO feed inlet. These results include (1) the pressure at the two accumulators, (2) the rate of change in feed pressure, and (3) the flow coefficient of the resistive element compared to the value determined from the feed-forward control law. A notable observation is that several instances are shown where the pressure upstream of the resistive element peaks to extreme values, yet these values are still well below the pressure relief valve setting of 20MPa. Another is that the rate of change in feed pressure and the valve coefficient command signal have higher frequency content that is not seen with the passive element. Finally, the feed-forward command signal for the flow coefficient has a mean value (543 L/s/$\mathrm{kPa}^{1/2}$) that is an order of magnitude greater than the maximum value (saturation limit) of 40 L/s/$\mathrm{kPa}^{1/2}$ that was chosen.

Finally, time-series results for the series-type architecture having 4370 liters of total accumulator volume are given in Fig. 8. This design has 1.12% of the accumulator volume placed at the RO feed inlet. These results include the pressure at the RO feed inlet and the pressure upstream of the hydraulic motor. The rate of change is not presented because it is near zero, being under direct control by the hydraulic motor. The RO feed pressure is controlled well and is nearly constant while the upstream pressure varies significantly. It is notable that the upstream pressure falls below the RO feed pressure for several periods within the simulation. In these cases, the hydraulic motor is in a pumping mode.

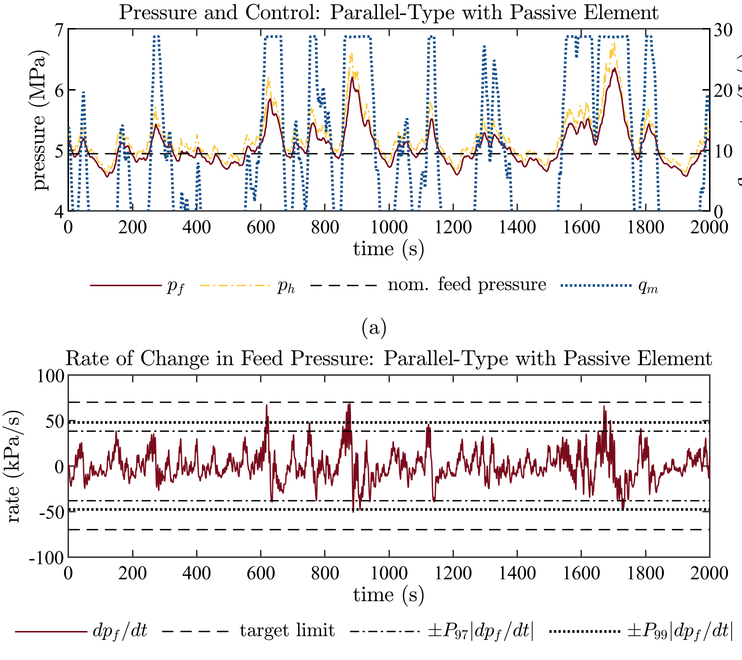

(a)

(b)

Fig. 6 Time-series results related to pressure variation for the parallel-type architecture with a passive resistive element: pressure and hydraulic motor flow rates (**a**) and rate of change in RO feed pressure (**b**)

5 Discussion

The results of this study suggest the series-type architecture is a superior design to the parallel-type architecture with respect to controlling the pressure variation at the RO module. This is in addition to this architecture using a 29% smaller WEC-driven pump, based on the results of the study presented in [23]. However, if the parallel-type architecture is chosen, adding a resistive-capacitive network to form a second-order low-pass filter can reduce the total accumulator volume by about half.

The results of this study also show that there is a significant cost associated with enforcing the 70 kPa/s constraint on the RO feed pressure rate of change. Treating the constraint as a hard limit in this study showed that an order of magnitude more accumulator volume is required than would be deployed otherwise. Yet the need for this constraint appears to be not well understood. Future work is needed to clarify what should be the constraints placed on the variation in pressure for wave-powered RO systems. Clarity on this issue will contribute significantly to our ability to design a robust and cost-effective system.

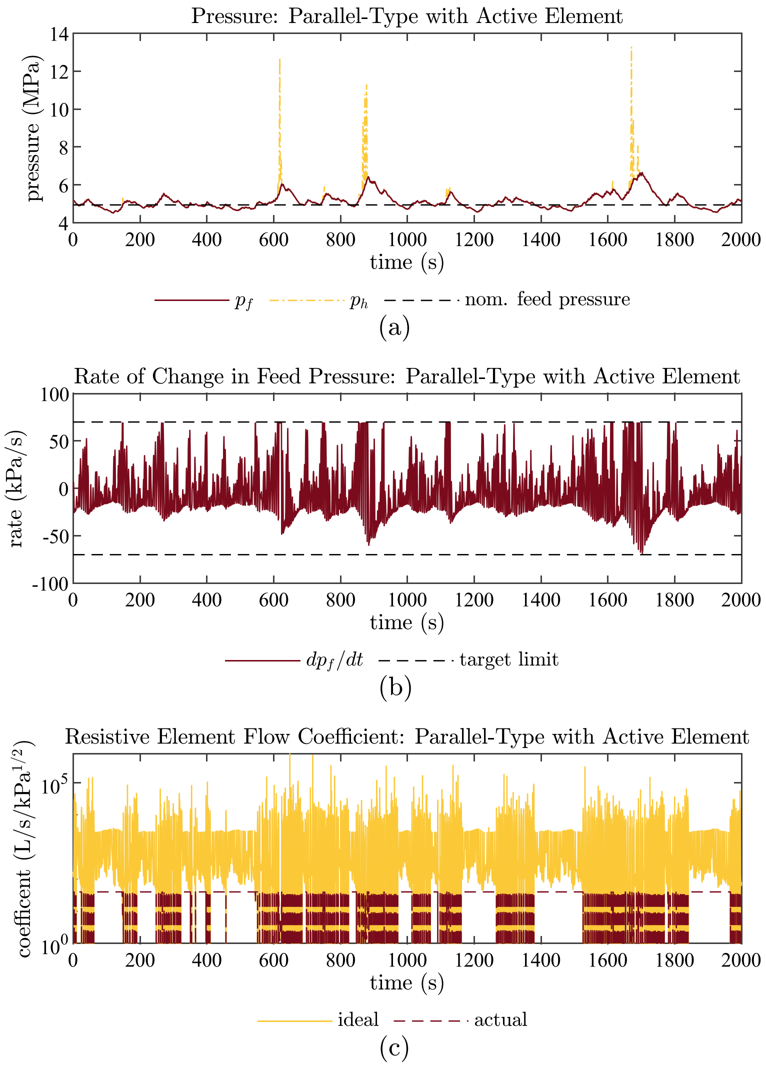

Fig. 7 Time-series results related to pressure variation for the parallel-type architecture with an active resistive element: pressure (**a**), rate of change in RO feed pressure (**b**), and flow coefficient of the resistive element (c)

A specific recommendation would be to clarify whether the rate of change in pressure contributes to mechanical failure or just degraded performance, whether that mechanism is accumulative, and to what degree. It was noted that the portion of time where peak rate of change is observed for the parallel-architecture is relatively small and that the 97th and 99th-percentile values for the rate of change are significantly lower than the peak. This highlights the fact that taking the limit of 70kPa/s as a

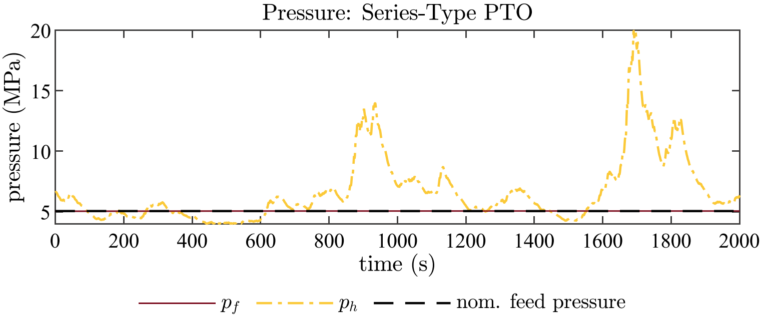

Fig. 8 Time-series results for pressure for the series-type PTO architecture

hard limit may be overly conservative. If a mechanism of failure or performance degradation is cumulative, a probabilistic distribution for the rate of change may be a more appropriate feature to consider in the design of these systems. If so, the system may tolerate a greater degree of pressure variation and require significantly less accumulator volume than observed in this study.

A trend in how accumulator volume is distributed in the system is illustrated by the study. Although the data are not given for all Pareto optimal results, the designs selected for comparison are representative of the trends between each architecture. Due to the direct control of flow at the RO feed inlet with the series-type architecture, very little accumulator volume, (i.e., 1.12%) is placed at the RO feed inlet. In contrast, 28.3% of the volume is placed at the RO feed inlet in the parallel-type architecture with the passive resistive element and 94.7% with the active resistive element. The active resistive element case is at the other extreme from the series-type PTO. This may be driven by the cases where the rate of change is negative, as in Fig. 7b at about 1700 s. In these cases, the resistive element is unable to force an increase in flow. This is where the active resistive element is limited; it is capable of retarding flow but not driving flow.

There may be room to further reduce the accumulator volume required by these systems. This study has assumed an accumulator charge pressure of 4 MPa regardless of the use case. The capacitance of an accumulator is greatly affected by charge pressure with it being more advantageous to have the charge pressure close to the operating pressure. Attention to this margin may yield a reduction in the required volume. This is especially notable for the series-type architecture where the upstream pressure is expected to be greater than the RO feed pressure. However, there likely needs to be a significant margin to accommodate the high level of flow and pressure variation in these systems. Another opportunity for reduced accumulator volumes is with higher working pressure limits since the pressure relief valves drive the increased power losses at low accumulator volumes.

A limitation of this study is that the design of this system was only examined for a single sea condition. The sea condition that was selected was argued to be a reasonable corner condition, but there is a motivation to extend that corner condition to higher energy sea states. This would require greater accumulator volumes than found in this study because of the higher peak power input to the system. Generally, the accumulator volume requirement is dominated by relatively infrequent sea conditions. A trade-off between production and component size requirements needs to be negotiated. This adds further motivation for clarifying and justifying the constraint. If the constraint were to be relaxed, this trade-off could be shifted toward higher production and lower accumulator volume requirements.

6 Conclusions

This study used numerical models to simulate the dynamics of a wave-powered RO system with a variety of power take-off architectures. A constraint found within the RO industry for the operation of an RO system is that the rate of change in feed pressure should not exceed 70 kPa/s. However, it is not clear what the mechanism of failure is that motivates the constraint. This study highlights the significance of this constraint in the design of a wave-powered RO system and the influence the power take-off architecture has on meeting this constraint. The results of this study showed that the constraint on the rate of change in feed pressure requires an order of magnitude greater high-pressure accumulator volume for the baseline system than if the constraint was not enforced. Furthermore, improvements over the baseline architecture were demonstrated for three proposed architectures. The study found that the addition of a resistive-capacitive network in the hydraulic circuit reduced the required high-pressure accumulator volume by 48% when the resistive element was passive and 55% when the resistive element was actively controlled through feed-forward control. The study also found that a series-type architecture, where a hydraulic motor is placed in series with the RO module, provides a reduction of about 75% in required accumulator volume while also requiring a 29% smaller WEC-driven pump.

7 Data Availability

Custom software and data used in this work are available at: https://github.com/novaTehnika/2023-DynPTOModelDesignStudies/releases/tag/publications2024 (accessed 29 April 2024).

Acknowledgements This material is based upon work supported by the U.S. National Science Foundation under award No. CMMI-2206018. Any opinions, findings and conclusions or recommendations expressed in this material are those of the author(s) and do not necessarily reflect the views of the U.S. National Science Foundation.

References

1. American-Made Challenges (2020). https://americanmadechallenges.org/. Accessed 06 Jul 2020
2. Oyster 1 (2010). http://www.aquamarinepower.com/technologies/oyster-1/. Accessed 29 Nov 2010
3. Resolute Marine Energy (2019). http://www.resolutemarine.com/. Accessed 15 Apr 2019
4. WAVE Water Treatment Design Software (2023). https://www.dupont.com/water/resources/design-software.html. Accessed 21 Aug 2023
5. Wave Energy Prize Experimental Sea State Selection (2017) In: International conference on offshore mechanics and arctic engineering, vol 10. Ocean Renewable Energy. https://doi.org/10.1115/OMAE2017-62675
6. Babarit A, Delhommeau G (2015) Theoretical and numerical aspects of the open source BEM solver nemoh. In: 11th European wave and tidal energy conference (EWTEC2015)
7. Das TK, Folley M, Lamont-Kane P, Frost C (2024) Performance of a SWRO membrane under variable flow conditions arising from wave powered desalination. Desalination 571:117,069
8. Dupont: Filmtec™ Reverse Osmosis Membranes Technical Manual. Dupont Water Solutions, Edina, MN, USA (2023). Form No 45-D01504-en, Rev 16
9. Falnes J, Kurniawan A (2020) Ocean waves and oscillating systems: linear interactions including wave-energy extraction, vol 8. Cambridge University Press
10. Folley M, Suarez BP, Whittaker T (2008) An autonomous wave-powered desalination system. Desalination 220(1–3):412–421. https://doi.org/10.1016/j.desal.2007.01.044
11. Folley M, Whittaker T (2009) The cost of water from an autonomous wave-powered desalination plant. Renew Energy 34(1):75–81. https://doi.org/10.1016/j.renene.2008.03.009
12. García Rodríguez L (2003) Renewable energy applications in desalination: state of the art. Solar Energy 75(5):381–393. https://doi.org/10.1016/j.solener.2003.08.005
13. Ghaffour N, Missimer TM, Amy GL (2013) Technical review and evaluation of the economics of water desalination: current and future challenges for better water supply sustainability. Desalination 309:197–207. https://doi.org/10.1016/j.desal.2012.10.015
14. Greenlee LF, Lawler DF, Freeman BD, Marrot B, Moulin P (2009) Reverse osmosis desalination: water sources, technology, and today's challenges. Water Res 43(9):2317–2348. https://doi.org/10.1016/j.watres.2009.03.010
15. Hansen RH, Andersen TO, Pedersen HC (2011) Model based design of efficient power take-off systems for wave energy converters. In: Proceedings of the 12th scandinavian international conference on fluid power, Tampere, Finland, pp 18–20
16. Kalogirou SA (2005) Seawater desalination using renewable energy sources. Prog Energy Combust Sci 31(3):242–281. https://doi.org/10.1016/j.pecs.2005.03.001
17. Kucera J (2015) Reverse osmosis: industrial processes and applications. Scrivener Publishing, Salem, MA
18. Leijon J, Boström C (2018) Freshwater production from the motion of ocean waves—a review. Desalination 435:161–171. https://doi.org/10.1016/j.desal.2017.10.049
19. McCandlish D, Dorey RE (1984) The mathematical modelling of hydrostatic pumps and motors. Proceedings of the Institution of mechanical engineers, Part B: management and engineering manufacture, vol 198(3), pp 165–174. https://doi.org/10.1243/PIME_PROC_1984_198_062_02
20. Nolan G, Ringwood J (2006) Control of a heaving buoy wave energy converter for potable water production. In: 2006 IET Irish signals and systems conference, pp 421–426
21. Perez T, Fossen TI (2009) A matlab toolbox for parametric identification of radiation-force models of ships and offshore structures. Model Identif Control **30**(1), 1–15. https://doi.org/10.4173/mic.2009.1.1
22. Simmons JW (2024) Modeling and design of hydraulic power take-offs for ocean wave-powered reverse osmosis desalination. PhD thesis, University of Minnesota

23. Simmons JW, Van de Ven JD (2023) A comparison of power take-off architectures for wave-powered reverse osmosis desalination of seawater with co-production of electricity. Energies 16(21):7381
24. Simmons JW, Van de Ven JD (2023) Limits on the range and rate of change in power take-off load in ocean wave energy conversion: a study using model predictive control. Energies 16(16):5909
25. Sitterley KA, Cath TJ, Jenne DS, Yu YH, Cath TY (2022) Performance of reverse osmosis membrane with large feed pressure fluctuations from a wave-driven desalination system. Desalination 527:115–546. https://doi.org/10.1016/j.desal.2022.115546
26. Tedeschi E, Carraro M, Molinas M, Mattavelli P (2011) Effect of control strategies and power take-off efficiency on the power capture from sea waves. IEEE Trans Energy Convers 26(4):1088–1098. https://doi.org/10.1109/TEC.2011.2164798
27. Wilf M, Awerbuch L (2007) The guidebook to membrane desalination technology: reverse osmosis, nanofiltration and hybrid systems: process, design, applications and economics. Balaban Desalination Publications, L'Aquila, Italy
28. Yu YH, Jenne D (2017) Analysis of a wave-powered, reverse-osmosis system and its economic availability in the united states. In: International conference on offshore mechanics and arctic engineering, vol 57786. American Society of Mechanical Engineers, p V010T09A032
29. Yu YH, Jenne D (2018) Numerical modeling and dynamic analysis of a wave-powered reverse-osmosis system. J Mar Sci Eng 6(4):132. https://doi.org/10.3390/jmse6040132